New Journal of Physics
The open access journal at the forefront of physics
Deutsche Physikalische Gesellschaft DPG IOP Institute of Physics

PAPER • OPEN ACCESS

Quantum-spin-Hall topological insulator in a spring-mass system

IOP Publishing New J. Phys. 20 (2018) 123011 https://doi.org/10.1088/1367-2630/aaf341

New Journal of Physics
The open access journal at the forefront of physics
Deutsche Physikalische Gesellschaft DPG
IOP Institute of Physics
Published in partnership with: Deutsche Physikalische Gesellschaft and the Institute of Physics

PAPER

Quantum-spin-Hall topological insulator in a spring-mass system

Yun Zhou[1], Prabhakar R Bandaru[1] and Daniel F Sievenpiper[2]

[1] Department of Mechanical and Aerospace Engineering, University of California, San Diego, La Jolla, CA 92093, United States of America
[2] Department of Electrical and Computer Engineering, University of California, San Diego, La Jolla, CA 92093, United States of America

E-mail: pbandaru@ucsd.edu and dsievenpiper@eng.ucsd.edu

Keywords: topological insulator, elastic waveguides, quantum spin Hall effect, acoustic metamaterials

CrossMark

OPEN ACCESS

RECEIVED
16 October 2018

REVISED
17 November 2018

ACCEPTED FOR PUBLICATION
23 November 2018

PUBLISHED
14 December 2018

Abstract

It is proposed that a lattice, with constituent masses and spring constants, may be considered as a model system for topological matter. For instance, a relative variation of the inter- and intra-unit cell spring constants can be used to create, tune, and invert band structure. Such an aspect is obtained while preserving time reversal symmetry, and consequently emulates the quantum spin Hall effect. The modal displacement fields of the mass-spring lattice were superposed so to yield pseudospin fields, with positive or negative group velocity. Considering that harmonic oscillators are the basis of classical and quantum excitations over a range of physical systems, the spring-mass system yields further insight into the constituents and possible utility of topological material.

1. Introduction

Inspired by the discovery of topological phases and edge states in electronic materials [1, 2], the possibility of building related devices for the control of the propagation of light [3–9] and sound [10–18] is being extensively studied. The related device building blocks may harness three major types of topological phases analogous to those in condensed matter systems: quantum Hall effect (QHE) [19, 20], quantum spin Hall effect (QSHE) [21–23], and quantum valley Hall effect (QVHE) [24–27]. The QHE has chiral edge modes, and requires an external magnetic field to break time reversal symmetry (TRS), which may be accomplished in acoustic and photonic systems by adding gyroscopic material or external circulators [3, 10–12, 28]. The QSHE is amenable to TRS, associated with a pair of spin-locked helical modes, and is obtained by introducing strong spin–orbit coupling [5, 8, 13, 17, 18]. The QVHE generates valley-locked chiral edge states, and exploits the valley degrees of freedom [6, 29].

It would of much advantage and yield insight, to consider a harmonic oscillator point of view, quite common in physics, for invoking topological phases. In this respect, a discrete spring-mass based mechanical system, may constitute a model system for topological structure as related to phononic materials. For instance, QHE based topological insulators in spring-mass lattices may be created by adding circulating gyroscopes [11, 28], Coriolis force [30] or varying spring tension [31]. QVHE has been realized in such systems by alternating the mass at A and B sites of the unit cell of a mechanical graphene-like lattice [29]: figure 1(a). QSHE-like phenomena has also been explored in spring-mass lattices, through coupled pendula [32], and a mechanical granular graphene system [33]. However, many of these systems are difficult to implement in practical applications.

In this paper, we propose a two-dimensional spring-mass system, exemplifying a QSHE topological insulator, in the acoustic domain. Various trivial and non-trivial band structures may be originated by varying the masses (m) and the relative spring constants (k) in the associated lattice. In addition to exhibiting the topological features that have now become familiar to practitioners in the field, we indicate a novel spin degree of freedom. The related pseudospins are observed, in frequency domain analysis as the polarization of modal displacement field of masses in one unit cell: figure 1(a). TRS protected edge modes, incorporating the propagation of such pseudospins, are shown to exist. This structure may be representative of different phases of

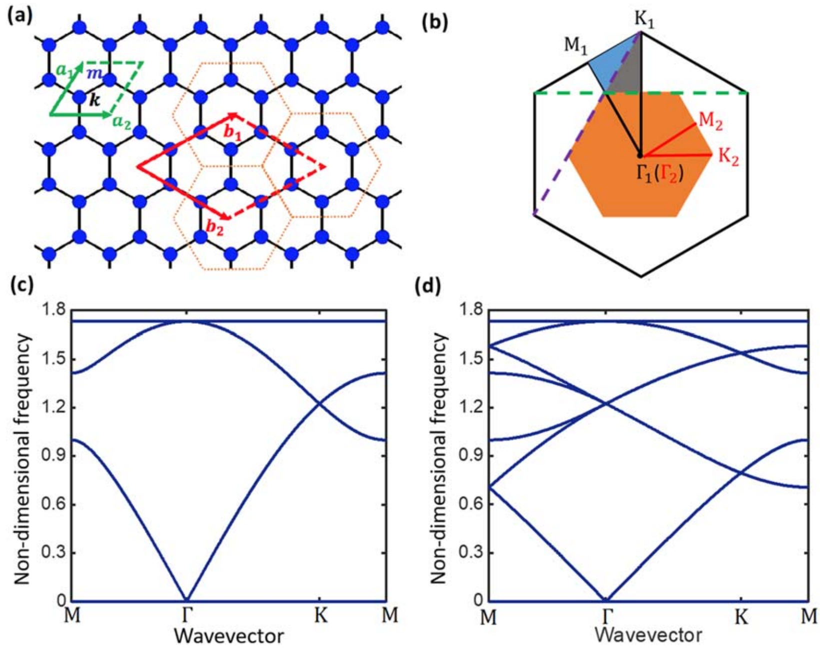

Figure 1. (a) Hexagonal spring-mass lattice with uniform spring constant k and mass m. a_1 and a_2 are lattice constants of the unit cell before zone folding, and b_1 and b_1 are lattice constants of the unit cell after zone folding. (b) First Brillouin zone (BZ) before (big hexagon) and after (small hexagon in orange) zone folding. When looking at 1/12 BZ, the triangle $\Gamma_1 M_1 K_1$ is first folded along the purple dashed line, then folded along the green dashed line. (c) Band diagram of the lattice in (a) for unit cell of 2 masses, and (d) band diagram of the lattice in (a) for the expanded unit cell of 6 masses.

matter, as the the spring constant can be view as coupling strength between unit cells in various systems. It can be applied as one of the possible practical designs of photonic/phononic topological insulators.

A basis for creating a topological material, based on a spring-mass system, to mimic the QSH effect, is to create intrinsic TRS. We consider a hexagonal lattice of masses and springs arranged in C_6 symmetry. The E and E' representations are each two-fold degenerate with the individuals being complex conjugates [34]. Consequently, a four-fold degeneracy is required to satisfy TRS and may be enabled through manifesting a double Dirac cone in the band structure. We achieve a four-fold degeneracy, in the band structure of a spring-mass constituted lattice by the zone-folding method [8].

2. The spring-mass model and computational methods

We consider a hexagonal lattice with equal masses m connected by linear springs k, as shown in figure 1(a). The unit cell of this hexagonal lattice consists of 2 masses $m^1 = m^2 = m$, with lattice constants $\overrightarrow{a_1}$ and $\overrightarrow{a_2}$ ($|\overrightarrow{a_1}| = |\overrightarrow{a_2}| = a$). From Newton's law, the governing equation $M\ddot{u} = F(u)$, where M is a diagonal matrix with the values of the two masses on its diagonal: $M = \mathrm{diag}\{m^1,\ m^1,\ m^2,\ m^2\}$. u is a vector constituted from the two degrees of freedom for each mass—the x and y direction displacements for m^1 and m^2: $u = \{u_x^1,\ u_y^1,\ u_x^2,\ u_y^2\}$ and F is the force. We consider a Bloch wave solution of the type $u = U\mathrm{e}^{\mathrm{i}(qa_1\gamma_1 + la_2\gamma_2 - \omega t)}$ to the governing equation of the $(q,\ l)$th unit cell, where $U = \{U_x^1,\ U_y^1,\ U_x^2,\ U_y^2\}$ is the modal displacement, and γ_1 and γ_2 are wave vectors. A dispersion relation is obtained by solving the eigenvalue problem $D(\gamma_1,\ \gamma_2)U = \omega^2 MU$, with D as a dynamical matrix (see appendix A).

The band structure of the hexagonal lattice in figure 1(c) exhibits a single Dirac cone at the $K\,(K')$ point. The frequencies are non-dimensionalized as $\Omega = \frac{\omega}{\sqrt{\frac{k}{m}}}$. Subsequently, we fold the first Brillouin zone (BZ) of the hexagonal lattice, twice, to form a new BZ with 1/3 of its original area, as shown in figure 1(b). Consequently, the $K\,(K')$ point is mapped to the Γ point at the center of the BZ, creating a double Dirac cone. The smaller BZ corresponds to an expanded unit cell in real space of 3 times of the original unit cell area, with $3 \times 2 = 6$ masses, and lattice constant $\overrightarrow{b_1}$ and $\overrightarrow{b_2}$ ($|\overrightarrow{b_1}| = |\overrightarrow{b_2}| = \sqrt{3}\,a = b$), as indicated in figure 1(a). The band structure based on the expanded unit cell is plotted in figure 1(d), and indicates a double Dirac cone at Γ.

To induce a phase transition, in the topological sense, we break the spatial symmetry of the hexagonal lattice, through changing the spring constants of the connecting masses in the lattice, i.e. distinguishing the intra unit cell spring constant k_1 from the inter unit-cell spring constant: k_2. Such distinction still preserves the C_6

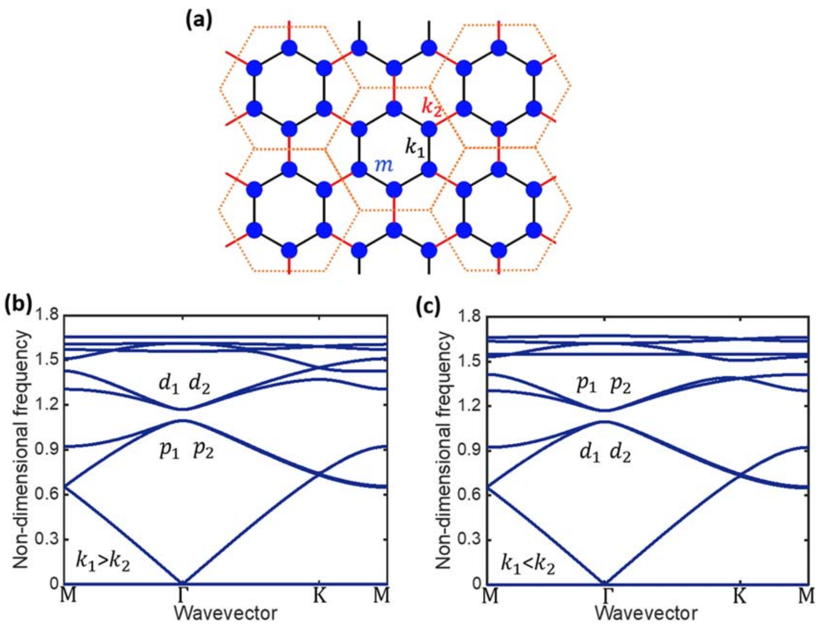

Figure 2. (a) Hexagonal spring-mass lattice with intra-cell spring k_1 (black straight rods) different from inter-cell spring k_2 (red straight rods). (b) Band diagram of hexagonal lattice with $k_1 > k_2$. Modal displacements at Γ are of *p* symmetry for the lower degeneracy, and of *d* symmetry for the higher degeneracy. (c) Band diagram of hexagonal lattice with $k_1 < k_2$. Modal displacements at Γ are of *d* symmetry for the lower degeneracy, and of *p* symmetry for the higher degeneracy.

symmetry of the unit cell. It was found that when $k_1 \neq k_2$, the band degeneracy at the Γ point is lifted and yields a band gap, as indicated in figures 2(b) and (c). With k_2 and m constant, we continuously change the value of k_1 from $k_1 > k_2$ to $k_1 < k_2$, through which the band gap at Γ point first closes and then reopens. When $k_1 = k_2$, there is no band gap (figures 2(a)–(c)). We study the modes related to this transition for (i) $k_1 > k_2$ and (ii) $k_1 < k_2$.

3. Results and discussions

3.1. Modal displacement fields in hexagonal spring-mass lattices: the case for pseudospins

The modal displacement and its *x* and *y* components, of the masses in the unit cell, at the Γ point of the $k_1 > k_2$ lattice are shown in figures 3(a)–(d). The labeling of the modes in figures 3(a)–(d) follows the nomenclature for the lower to higher band degeneracy corresponding to figure 2(b). The modal displacements for a given mass in $p_1(/d_1)$ are orthogonal to $p_2(/d_2)$, respectively. The constituent *x* and *y* direction displacements are plotted successively below. Since each mass has two degrees of freedom—the displacements in the *x*- and the *y*-directions, in considering the parities of modal displacements in figure 3, we consider the *x*- and the *y*-direction modal displacement fields separately. We find that the *x/y* direction displacements fields at Γ are of odd and even spatial parities—of the p_x $(/p_y)$ and $d_{x^2-y^2}$ $(/d_{xy})$ variety, as inferred both from the sense of the symmetry of the displacements and stated relationships in the C_6 character table [34]. For instance, the p_x $(/p_y)$ character is antisymmetric with respect to the center, even symmetric to the *x*- (/*y*-) axis, and odd symmetric to the *y*- (/*x*-) axis, while the $d_{x^2-y^2}$ $(/d_{xy})$ parity is symmetric with repsect to the center, and even(/odd) symmetric to both the *x* and *y* axes.

Hybridizing the p_1/d_1 and p_2/d_2 modes in a symmetric and antisymmetric manner yields pseudospins [8]

$$p_\pm = (p_1 \pm \mathrm{i}p_2/\sqrt{2}), \text{ and } d_\pm = (d_1 \pm \mathrm{i}d_2)/\sqrt{2}. \tag{1}$$

Figures 3(e)–(h) illustrates the related phase distribution of p_+, p_-, d_+ and d_- in the range of $-\pi$ to π (see appendix B). Clearly seen from the phase relationship that harmonic wave propagation in p_+/d_+ and p_-/d_- have opposite polarizations. Taking the time harmonic component $\mathrm{e}^{\mathrm{i}\omega t}$ into consideration, due to the orthogonality of displacements in p_1/d_1 and p_2/d_2, each mass corresponding to the hybridized mode p_+/d_+ rotates in the one direction, while each mass in p_-/d_- rotates in the opposite direction. The incorporation of the relative motions of the six masses in the unit cell leads to rotation of the whole displacement field. Such rotation may be

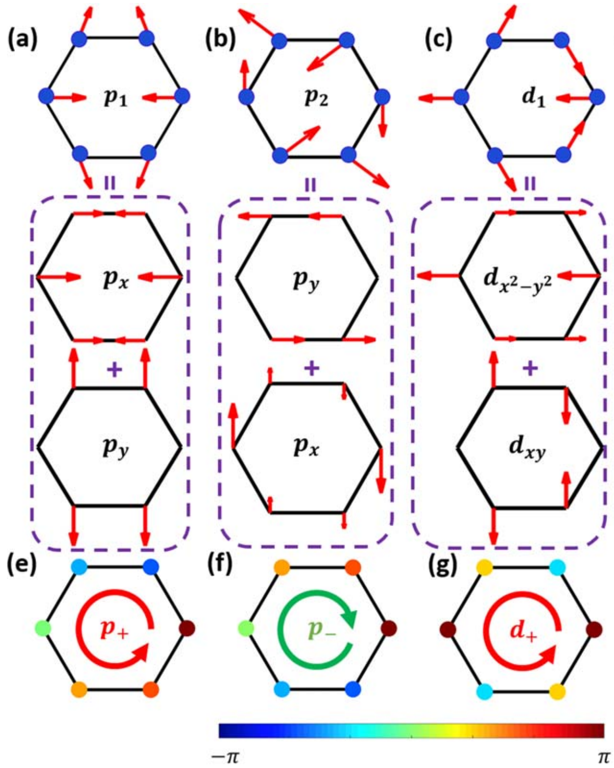

Figure 3. (a) p_1, (b) p_2 and (c) d_1, (d) d_2 are total modal displacements for the two two-fold degeneracies at Γ point when $k_1 \neq k_2$. p_1 and p_2 have odd parities, while d_1 and d_2 have even parities. x and y direction components to (a) and (b) clearly show p_x/p_y symmetry, while those to (c) and (d) that have $d_{x^2-y^2}/d_{xy}$ symmetry. (e)–(h) are plots of phase relationships between the 6 masses in one unit cell for p_+, p_-, d_+ and d_- in color map, indicating the polarization of wave propagation associated with pseudospin up and pseudospin down.

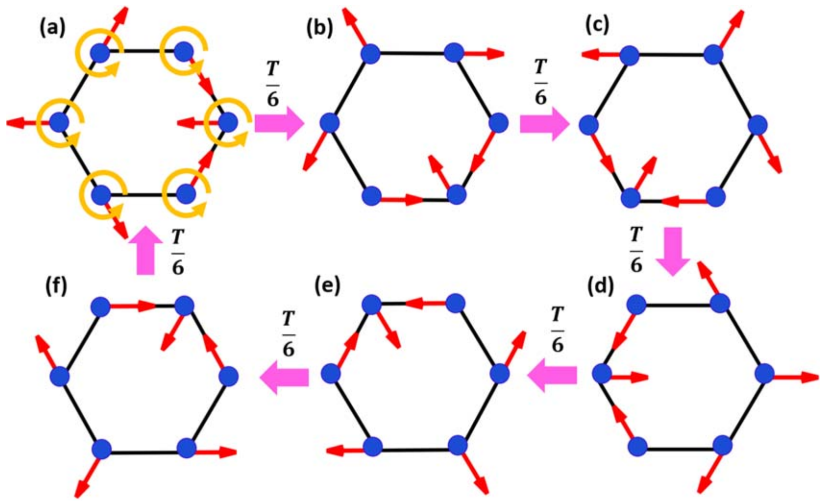

Figure 4. The spinning of modal displacement field for $d_+ = (d_1 + \mathrm{i}d_2)/\sqrt{2}$ as a result of time domain motion of the masses during one period T.

considered as one manifestation of a pseudo-spin. One can follow the motion in d_+ during one time period T: figure 4, indicating such clockwise orientability of the displacement field.

We find that for the case of $k_1 < k_2$, the modal displacement fields have exactly the same odd and even spatial parities, but d_1 and d_2 are now associated with the higher two degenerate bands, while p_1 and p_2 corresponds to the lower two bands (figure 2(c)). This demonstrates that band inversion happens at the Γ point during the process of closing and reopening the band gap, and a change in topology of the band structure. Such a change has

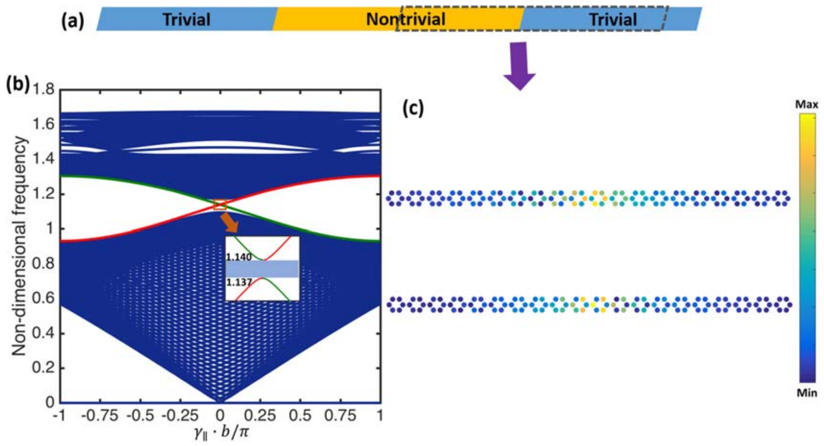

Figure 5. (a) Ribbon super cell consists of 20 non-trivial unit cells cladded by 15 trivial unit cells on each end. The mases and springs are of the ratio $\frac{m^{\mathrm{T}}}{m^{\mathrm{NT}}} = \frac{1.315}{1}$ and k_1^{T}: k_2: $k_1^{\mathrm{NT}} = 1.2{:}\ 1{:}\ 0.8$, respectively. (b) The band diagram for the ribbon super cell. A pair of pseudospin up and pseudospin down edge modes are found within the bulk band gap (red and green curves). The inset shows a mini band gap at the crossing of the two helical modes. Magnitude of modal displacements of the pseudospin up and pseudospin down modes near the right boundary at $\gamma_{\|} = 0.1\frac{\pi}{b}$ are plotted in (c), from which we can see that they are confined at the edge and decay into the bulk.

been previously quantified through the spin Chern number [35]. The Hamiltonian on the basis states of $[p_+,\ d_+,\ p_-,\ d_-]$ can be obtained (see appendix C) to be of the following form:

$$H^{\mathrm{eff}}(\gamma) = \begin{bmatrix} M - B\gamma^2 & A\gamma_+ & 0 & 0 \\ A^*\gamma_- & -M + B\gamma^2 & 0 & 0 \\ 0 & 0 & M - B\gamma^2 & A\gamma_- \\ 0 & 0 & A^*\gamma_+ & -M + B\gamma^2 \end{bmatrix}, \tag{2}$$

where $\gamma_\pm = \gamma_x \pm \mathrm{i}\gamma_y$, and $\gamma^2 = {\gamma_x}^2 + {\gamma_y}^2$. $A = \mathrm{i}\alpha k_2$ is imaginary ($\alpha > 0$), and $B < 0$. $M = \dfrac{\varepsilon_d - \varepsilon_p}{2}$ indicates the relative energy of p and d bands, which is positive in the lattice of $k_1 > k_2$, and negative in the lattice of $k_1 < k_2$, respectively. The spin Chern number can be calculated from

$$C_S = \pm\frac{1}{2}(\mathrm{sgn}(M) + \mathrm{sgn}(B)). \tag{3}$$

Since B is negative, C_s depends on the sign of M, which leads to $C_s = 0$ when $M > 0$, and $C_s = \pm 1$ when $M < 0$. This means that for the lattice with $k_1 > k_2$, $C_s = 0$, and the band gap is topologically trivial (figure 2(b)). When we decrease k_1 to $k_1 < k_2$, the band gap becomes topologically non-trivial (figure 2(c)) and $C_s = \pm 1$. Therefore, from the topological band theory [1] it would be expected that there would exist pseudospin-dependent edge modes at the boundary between topologically trivial and topologically non-trivial lattices.

3.2. Propagating edge modes

The pseudospin-dependent edge modes are vividly illustrated through simulations on a ribbon-shaped lattice that is periodic in one direction and of the width of one unit cell in the other direction: figure 5(a). Such a supercell based lattice contains both topologically trivial (T) and non-trivial (NT) units. The NT lattice is constituted from one row of 20 unit cells, and cladded by two T units of 15 unit cells (we chose the number of T and NT units so that the band diagram is relatively scale invariant). Here, the masses in the T and NT units lattice are in the ratio $\frac{m^{\mathrm{T}}}{m^{\mathrm{NT}}} = \frac{1.315}{1}$, and spring constants are of the ratio k_1^{T}: k_2: $k_1^{\mathrm{NT}} = 1.2{:}\ 1{:}\ 0.8$. The inter-cell spring constant k_2 is kept the same in both the T and NT units since it connects the two different lattices. The spring constants and masses were chosen such that the T and the NT units have overlapped band gap as related to the frequency ranges indicated in figures 2(b) and (c). The band structure of the ribbon supper cell is shown in figure 5(b) (the frequencies here are non-dimensionalized as $\Omega = \frac{\omega}{\sqrt{\frac{k_2}{m^{\mathrm{NT}}}}}$). Compared to the band structures in figure 2(b) and (c), we clearly see two additional states appear within the bulk band gap connecting the lower bands to the higher bands, as illustrated by red and green lines in figure 5(b). It was noted that these two new

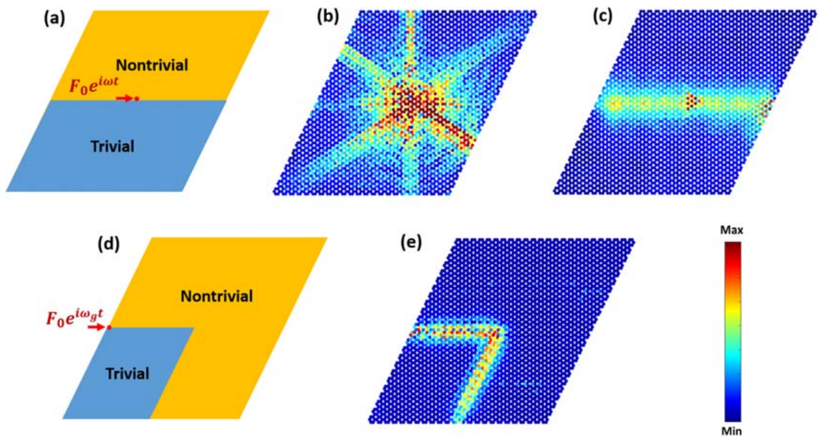

Figure 6. Time domain simulation of edge wave propagation. The domain is of 24 by 24 unit cells. The mases and springs are of the ratio $\frac{m^{\mathrm{T}}}{m^{\mathrm{NT}}} = \frac{1.315}{1}$ and k_1^{T}: k_2: $k_1^{\mathrm{NT}} = 1.2$: 1: 0.8, respectively. (a) Sinusoidal excitation force $F = F_0 \mathrm{e}^{\mathrm{i}\omega t}$ applied on a line edge between topologically non-trivial and trivial spring-mass lattices. (b) and (c) are the simulation results with $\omega = \omega_b = 0.8\sqrt{\frac{k_2}{m^{\mathrm{NT}}}}$ (frequency within the bulk bands), and $\omega = \omega_g = 1.14\sqrt{\frac{k_2}{m^{\mathrm{NT}}}}$ (frequency within the bulk band gap). (d) Is a spring-mass lattice that contains a topological edge with a sharp turning, and (e) simulation result on (d) with a force excitation of frequency ω_g.

modes propagate with a group velocity of the same magnitude but opposite signs, and correspond to the pseudospin up and pseudospin down topological edge modes. There is a mini band gap at the Γ point of the zoomed-in band structure in the inset of figure 5(b), due to breaking of C_6 symmetry at the boundary of the T and the NT units (see appendix D). However, this mini band gap is much smaller compared to the bulk band gap (0.003:0.08), so the pseudospins are preserved, and backscattering of edge states is suppressed as shown in the time-domain simulations below. We plotted the modal displacement corresponding to the two additional states of the ribbon lattice near the Γ point ($\gamma_{||} = 0.1\frac{\pi}{b}$, b is the lattice constant of the extended unit cell) in figure 5(c). These modes are confined to the boundary between the T and the NT units, and decay into the bulk, indicative of edge mode-like character. The appearance of such modes, in the absence of any obvious spin–orbit coupling indicates attributes of a QSHE topological insulator.

To verify the unidirectional propagation of the topological edge modes, we conducted time-domain numerical simulations on finite spring-mass lattices consists of both T and NT units. The governing equation for the spring-mass lattice takes the form $\ddot{u} = Au + F(t)$, where Au is the restoring/displacement-dependent force due to spring deformations, and $F(t)$ is a time-dependent excitation. We solve the equivalent ODE: $\begin{bmatrix} \ddot{u} \\ \dot{u} \end{bmatrix} = AA\begin{bmatrix} \dot{u} \\ u \end{bmatrix} + F(t)$, where $AA = \begin{bmatrix} 0 & A \\ I & 0 \end{bmatrix}$($I$ is unitary matrix), using Runge–Kutta explicit time integration method (RK4) to determine the displacement u at time t. Fixed boundary conditions were applied in the simulations, i.e. masses at the boundaries are connected to springs fixed to the wall.

Figure 6(a) shows the geometry of the modeled spring-mass lattice consisting of a NT and T unit, at the top and bottom, respectively. Initially all the masses are at rest. To avoid boundary reflection, we enforced an excitation force $F(t) = F_0 \mathrm{e}^{\mathrm{i}\omega t}$ on one of the masses in the NT unit close to the middle of the NT–T boundary, with frequency $\omega = \omega_b = 0.8\sqrt{\frac{k_2}{m^{\mathrm{NT}}}}$ corresponding to that of the bulk (from the T/NT band structure), and $\omega = \omega_g = 1.14\sqrt{\frac{k_2}{m^{\mathrm{NT}}}}$ corresponding to within the band gap, respectively (for example, a lattice with $m^{\mathrm{NT}} = 1$ kg, $k_2 = 10^6$ N m^{-1}, $\omega_b = 800$ Hz, and $\omega_g = 1140$ Hz). The simulation results in figures 6(b) and (c) indicate the amplitude of displacement of the masses, and illustrate that an external force (with $\omega = \omega_b$) will propagate into the bulk, while a force (with $\omega = \omega_g$) will only excite states that propagate at the edge of the T and NT domains. A sharp discontinuity turning boundary between T and NT as indicated in figure 6(d) demonstrates that the edge states were immune to backscattering figure 6(e).

As the indicated pseudospins are symmetrized configurations of modal displacement fields, they are not prone to selective and individual excitation. However, in another application of the T–NT unit arrangement shown in figure 7(a), it may be able to separate out the counter-propagating states, as broadly constructed in figures 3(e)–(h). With $F = F_0 \mathrm{e}^{\mathrm{i}\omega t}$ it was seen that when a left-moving state (say, with positive group velocity) reaches the crossing, it will propagate up to port 1 and down to port 2 along the edges but will not propagate right to the port 3. Consequently, the trajectory of wave propagation (figures 7(b)–(f)) forms a 'T' shape. It

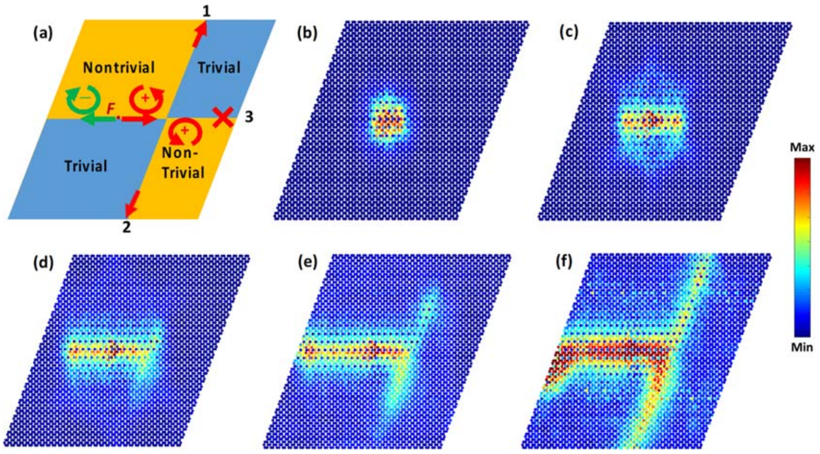

Figure 7. Pseudospin-dependent wave transport in a waveguide splitter. (a) Waveguide splitter divided into 4 parts, with top left and bottom right of non-trivial lattice, and top right and bottom left of trivial lattice. The cross has angle of 60° to keep the unit cells intact. An excitation force with frequency within the band gap can excite both pseudospin-up and pseudospin down modes. Pseudospin-up modes are supported to propagate towards the right, but splits into 2 waves at the cross, that exit from port 1 and 2, respectively. But it is forbidden to exit from port 3, as right-propagate pseudospin-up modes are not supported by the domain to the right of the cross. (b)–(f) are snapshots of time domain simulation at $t = 2000t_0$, $4000t_0$, $6000t_0$, $8000t_0$ and $10000t_0$, where t_0 is the time step of the simulation.

was noted that the excited modes are sensitive to boundary conditions, that leads to high amplitude at the boundary.

4. Conclusions

In summary, we have shown that a mass-spring based lattice system may have attributes related to that of a topological insulator, in the presence of TRS. Through varying the inter- and inter-unit cell spring constants of such a lattice, for a given mass, a clear and distinct variation of the band structure was seen. A concomitant change in the modal displacement fields, corresponding to a band inversion, may be generated. The deconvolution of the fields as well as their hybridization in a symmetric and antisymmetric manner yields a basis for the creation of pseudo-spins, corresponding to clockwise/counter-clockwise rotation of the modal displacement vector. Both pseudo spin-up and pseudo spin-down modalities, corresponding to the positive or negative group velocity are proposed. The existence of polarized edge states as well as corresponding modes was demonstrated through both frequency domain analysis and time domain simulations. These edge modes are topologically protected, as they are immune to backscattering when encountering sharp edges. Considering that harmonic oscillators (which are direct manifestations of spring-mass units) form the basis for many physical systems, ranging from acoustics to electromagnetics, this work yields a general foundational framework and related methodology, i.e. modulating band structure and constituent modes through varying the respective spring constants of the physical system.

Acknowledgments

This work was supported by ARO grant No. W911NF-17-1-0453. The authors acknowledge discussions with D Bisharat and X Kong.

Appendix A. Dynamical matrix for spring-mass lattice

To get the dispersion relations, we evaluate

$$Du = \omega^2 u, \tag{4}$$

where D is the dynamical matrix, and u is the displacements of the masses.

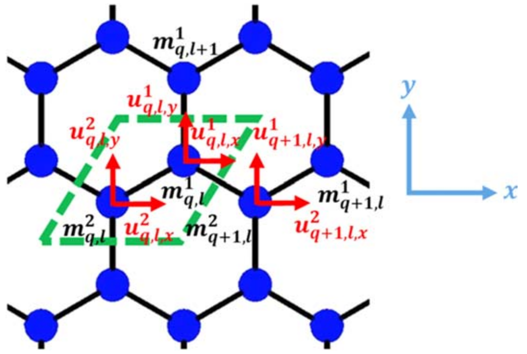

Figure 8. Hexagonal spring-mass lattice with uniform spring constant k and mass m. Unit cell $(q,\ l)$ consist of two masses $m^1_{q,l}$ and $m^2_{q,l}$.

For a two-mass unit cell shown in figure 8, D is derived to be of form

$$D(\gamma_1,\ \gamma_2) = -\begin{bmatrix} -\frac{3}{2}k & 0 & \frac{3}{4}(1 + \mathrm{e}^{\mathrm{i}\gamma_1})k & \frac{\sqrt{3}}{4}(1 - \mathrm{e}^{\mathrm{i}\gamma_1})k \\ 0 & -\frac{3}{2}k & \frac{\sqrt{3}}{4}(1 - \mathrm{e}^{\mathrm{i}\gamma_1})k & \left(\frac{1}{4} + \frac{1}{4}\mathrm{e}^{\mathrm{i}\gamma_1} + \mathrm{e}^{\mathrm{i}\gamma_2}\right)k \\ \frac{3}{4}(1 + \mathrm{e}^{-\mathrm{i}\gamma_1})k & \frac{\sqrt{3}}{4}(1 - \mathrm{e}^{-\mathrm{i}\gamma_1})k & -\frac{3}{2}k & 0 \\ \frac{\sqrt{3}}{4}(1 - \mathrm{e}^{-\mathrm{i}\gamma_1})k & \left(\frac{1}{4} + \frac{1}{4}\mathrm{e}^{-\mathrm{i}\gamma_1} + \mathrm{e}^{-\mathrm{i}\gamma_2}\right)k & 0 & -\frac{3}{2}k \end{bmatrix}. \tag{5}$$

The elements of D were obtained through assuming a Bloch wave solution of form $u_{q,l} = U\mathrm{e}^{\mathrm{i}(qa_1\gamma_1 + la_2\gamma_2 - \omega t)}$. Here $U = \{U^1_x,\ U^1_y,\ U^2_x,\ U^2_y\ \}$ is the modal displacement vector, and γ_1 and γ_2 are Bloch wave vectors. Take the mass $m^1_{q,l}$ in unit cell $(q,\ l)$ for example. The force balance for $m^1_{q,l}$ in x direction can be written as

$$m^1_{q,l}\ddot{u}^1_{q,l,x} = k\Big[(u^2_{q+1,l,x} - u^1_{q,l,x})\cos\frac{\pi}{6}\cos\frac{\pi}{6} + (u^1_{q,l,y} - u^2_{q,l+1,y})\sin\frac{\pi}{6}\cos\frac{\pi}{6} + (u^2_{q,l,x} - u^1_{q,l,x})\cos\frac{\pi}{6}\cos\frac{\pi}{6} + (u^2_{q,l,y} - u^1_{q,l,y})\sin\frac{\pi}{6}\cos\frac{\pi}{6}\Big]. \tag{6}$$

Substitute the Bloch solution into equation (6) we get

$$-\omega^2 m^1_{q,l}U^1_x = -\frac{3}{2}kU^1_x + 0U^1_y + \frac{3}{4}(1 + \mathrm{e}^{\mathrm{i}\gamma_1})kU^2_x + \frac{\sqrt{3}}{4}(1 - \mathrm{e}^{\mathrm{i}\gamma_1})kU^2_y, \tag{7}$$

which are elements of the first raw of equation (5). Other entries of D can be obtained in a similar manner.

Appendix B. Phase relationship for masses in one unit cell for pseudo spin modes

Modal displacement for each mass in the unit cell in $p_\pm = p_1 \pm \mathrm{i}p_2$ and $d_\pm = d_1 \pm \mathrm{i}d_2$ are complex numbers. We take the phase angle of the displacement for each mass and plot the phase relation of the unit cell as shown in figures 3(e)–(h).

Take $d_+ = d_1 + \mathrm{i}d_2$ for example. From the eigenvalue problem of the dynamical matrix in equation (8), when $k_1 = 0.8\ \mathrm{N\ m^{-1}}$, $k_2 = 1\ \mathrm{N\ m^{-1}}$, and $m = 1$ kg, we have the values (in meter) of x- and y- direction modal displacements for each mass in d_1 and d_2 shown as figure 9. The modal displacements and phase relation for d_+ can be calculated accordingly. As shown in figure 9, phase plots for x- and y- direction modal displacement fields show same polarization, and both have the change of 4π in one unit cell, indicative of even parity/quadruple symmetries.

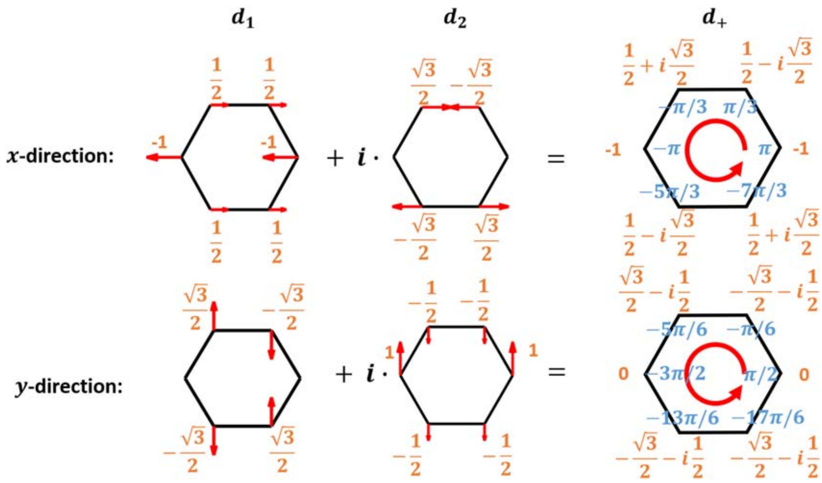

Figure 9. Phase relationship between masses in one unit cell for mode $d_+ = d_1 + id_2$.

Appendix C. Effective Hamiltonian, Berry curvature, spin Chern number, and Z_2 invariant

The dynamical matrix D for 6 masses with 12 constituent modal displacements (i.e. $U = [U_x^1,\ U_y^1,\ U_x^2,\ U_y^2,\ U_x^3,\ U_y^3,\ U_x^4,\ U_y^4,\ U_x^5,\ U_y^5,\ U_x^6,\ U_y^6]^T$) is of the form:

$$D = \left[\begin{array}{cccccccccccc}
\frac{3}{2}\frac{k_2}{m} & 0 & -\frac{3}{4}\frac{k_1}{m} & \frac{\sqrt{3}}{4}\frac{k_1}{m} & 0 & 0 & 0 & 0 & 0 & 0 & -\frac{3}{4}\frac{k_1}{m} & -\frac{\sqrt{3}}{4}\frac{k_1}{m} \\
0 & \frac{k_2}{m}+\frac{1}{2}\frac{k_1}{m} & \frac{\sqrt{3}}{4}\frac{k_1}{m} & -\frac{1}{4}\frac{k_1}{m} & 0 & 0 & 0 & -\frac{k_2}{m}e^{i\gamma_2} & 0 & 0 & -\frac{\sqrt{3}}{4}\frac{k_1}{m} & -\frac{1}{4}\frac{k_1}{m} \\
-\frac{3}{4}\frac{k_1}{m} & \frac{\sqrt{3}}{4}\frac{k_1}{m} & \frac{3}{4}\frac{k_1}{m}+\frac{3}{4}\frac{k_2}{m} & -\frac{\sqrt{3}}{4}\left(\frac{k_1}{m}-\frac{k_2}{m}\right) & 0 & 0 & 0 & 0 & -\frac{3}{4}\frac{k_2}{m}e^{i\gamma_1} & -\frac{\sqrt{3}}{4}\frac{k_2}{m}e^{i\gamma_1} & 0 & 0 \\
\frac{\sqrt{3}}{4}\frac{k_1}{m} & -\frac{1}{4}\frac{k_1}{m} & -\frac{\sqrt{3}}{4}\left(\frac{k_1}{m}-\frac{k_2}{m}\right) & \frac{1}{4}\frac{k_2}{m}+\frac{5}{4}\frac{k_1}{m} & 0 & -\frac{k_1}{m} & 0 & 0 & -\frac{\sqrt{3}}{4}\frac{k_2}{m}e^{i\gamma_1} & -\frac{1}{4}\frac{k_2}{m}e^{i\gamma_1} & 0 & 0 \\
0 & 0 & 0 & 0 & \frac{3}{4}\frac{k_1}{m}+\frac{3}{4}\frac{k_2}{m} & \frac{\sqrt{3}}{4}\left(\frac{k_1}{m}-\frac{k_2}{m}\right) & -\frac{3}{4}\frac{k_1}{m} & -\frac{\sqrt{3}}{4}\frac{k_1}{m} & 0 & 0 & -\frac{3}{4}\frac{k_2}{m}e^{i\gamma_1-i\gamma_2} & -\frac{1}{4}\frac{k_2}{m}e^{i\gamma_1-i\gamma_2} \\
0 & 0 & 0 & -\frac{k_1}{m} & \frac{\sqrt{3}}{4}\left(\frac{k_1}{m}-\frac{k_2}{m}\right) & \frac{1}{4}\frac{k_2}{m}+\frac{5}{4}\frac{k_1}{m} & -\frac{\sqrt{3}}{4}\frac{k_1}{m} & -\frac{1}{4}\frac{k_1}{m} & 0 & 0 & \frac{\sqrt{3}}{4}\frac{k_2}{m}e^{i\gamma_1-i\gamma_2} & \frac{\sqrt{3}}{4}\frac{k_2}{m}e^{i\gamma_1-i\gamma_2} \\
0 & 0 & 0 & 0 & -\frac{3}{4}\frac{k_1}{m} & -\frac{\sqrt{3}}{4}\frac{k_1}{m} & \frac{3}{2}\frac{k_2}{m} & 0 & -\frac{3}{4}\frac{k_1}{m} & \frac{\sqrt{3}}{4}\frac{k_1}{m} & 0 & 0 \\
0 & -\frac{k_2}{m}e^{-i\gamma_2} & 0 & 0 & -\frac{\sqrt{3}}{4}\frac{k_1}{m} & -\frac{1}{4}\frac{k_1}{m} & 0 & \frac{k_2}{m}+\frac{1}{2}\frac{k_1}{m} & \frac{\sqrt{3}}{4}\frac{k_1}{m} & -\frac{1}{4}\frac{k_1}{m} & 0 & 0 \\
0 & 0 & -\frac{3}{4}\frac{k_2}{m}e^{-i\gamma_1} & -\frac{\sqrt{3}}{4}\frac{k_2}{m}e^{-i\gamma_1} & 0 & 0 & -\frac{3}{4}\frac{k_1}{m} & \frac{\sqrt{3}}{4}\frac{k_1}{m} & \frac{3}{4}\frac{k_1}{m}+\frac{3}{4}\frac{k_2}{m} & -\frac{\sqrt{3}}{4}\left(\frac{k_1}{m}-\frac{k_2}{m}\right) & 0 & 0 \\
0 & 0 & -\frac{\sqrt{3}}{4}\frac{k_2}{m}e^{-i\gamma_1} & -\frac{1}{4}\frac{k_2}{m}e^{-i\gamma_1} & 0 & 0 & \frac{\sqrt{3}}{4}\frac{k_1}{m} & -\frac{1}{4}\frac{k_1}{m} & -\frac{\sqrt{3}}{4}\left(\frac{k_1}{m}-\frac{k_2}{m}\right) & \frac{1}{4}\frac{k_2}{m}+\frac{5}{4}\frac{k_1}{m} & 0 & -\frac{k_1}{m} \\
-\frac{3}{4}\frac{k_1}{m} & -\frac{\sqrt{3}}{4}\frac{k_1}{m} & 0 & 0 & -\frac{3}{4}\frac{k_2}{m}e^{-i\gamma_1+i\gamma_2} & \frac{\sqrt{3}}{4}\frac{k_2}{m}e^{-i\gamma_1+i\gamma_2} & 0 & 0 & 0 & 0 & \frac{3}{4}\frac{k_1}{m}+\frac{3}{4}\frac{k_2}{m} & \frac{\sqrt{3}}{4}\left(\frac{k_1}{m}-\frac{k_2}{m}\right) \\
-\frac{\sqrt{3}}{4}\frac{k_1}{m} & -\frac{1}{4}\frac{k_1}{m} & 0 & 0 & \frac{\sqrt{3}}{4}\frac{k_2}{m}e^{-i\gamma_1+i\gamma_2} & -\frac{1}{4}\frac{k_2}{m}e^{-i\gamma_1+i\gamma_2} & 0 & 0 & 0 & -\frac{k_1}{m} & \frac{\sqrt{3}}{4}\left(\frac{k_1}{m}-\frac{k_2}{m}\right) & \frac{1}{4}\frac{k_2}{m}+\frac{5}{4}\frac{k_1}{m}
\end{array}\right] \tag{8}$$

There are 12 bands corresponding to the 12 by 12 matrix D. To investigate the spin-Chern number, we derive the effective Hamiltonian [36] assuming that the other 8 bands have negligible influence. Modal displacement vector U can be rewritten as the superposition of p_1, p_2, d_1, and d_2: $U' = c_1 p_1 + c_2 p_2 + c_3 d_1 + c_4 d_2$, where c_1, c_2, c_3, and c_4 are coefficients. Based on these assumptions, equation (4) gives

$$DU' = \begin{bmatrix} \omega_p^2 & 0 & 0 & 0 \\ 0 & \omega_p^2 & 0 & 0 \\ 0 & 0 & \omega_d^2 & 0 \\ 0 & 0 & 0 & \omega_d^2 \end{bmatrix} U'. \tag{9}$$

From this we get the 4 by 4 effective Hamiltonian on the basis of $[p_1\ p_1\ d_1\ d_2]$ as

$$H = [p_1\ p_2\ d_1\ d_2]^\dagger D [p_1\ p_2\ d_1\ d_2]. \tag{10}$$

And the eigenvalue problem can be written as

$$H\begin{bmatrix} c_1 \\ c_2 \\ c_3 \\ c_4 \end{bmatrix} = \begin{bmatrix} \omega_p^2 & 0 & 0 & 0 \\ 0 & \omega_p^2 & 0 & 0 \\ 0 & 0 & \omega_d^2 & 0 \\ 0 & 0 & 0 & \omega_d^2 \end{bmatrix}\begin{bmatrix} c_1 \\ c_2 \\ c_3 \\ c_4 \end{bmatrix}. \tag{11}$$

(Since p_1, p_2, d_1, and d_2 are normalized and orthogonal vectors, $[p_1\ p_2\ d_1\ d_2]^\dagger [p_1\ p_2\ d_1\ d_2] = I$.) Each element in H can be approximated to the second order using Taylor expansion.

For lattice with $k_1 < k_2$, take $k_1 = 0.8$, $k_2 = 1$ and $m = 1$. Neglect second-order off-diagonal terms, the effective Hamiltonian is (here $\gamma_x = \gamma_1 - \dfrac{1}{2}\gamma_2$ and $\gamma_y = \dfrac{\sqrt{3}}{2}\gamma_2$)

$$H_{\mathrm{NT}} = \begin{bmatrix} \omega_p^2 - 0.168k_2\left(\gamma_x^2 + \frac{1}{3}\gamma_y^2\right) & 0 & 0.2387\mathrm{i}k_2\gamma_y & 0.2387\mathrm{i}k_2\gamma_x \\ 0 & \omega_p^2 - 0.168k_2\left(\frac{1}{3}\gamma_x^2 + \gamma_y^2\right) & -0.2387\mathrm{i}k_2\gamma_x & 0.2387\mathrm{i}k_2\gamma_y \\ -0.2387\mathrm{i}k_2\gamma_y & 0.2387\mathrm{i}k_2\gamma_x & \omega_d^2 + 0.25k_2\left(\gamma_x^2 + \frac{1}{3}\gamma_y^2\right) & 0 \\ -0.2387\mathrm{i}k_2\gamma_x & -0.2387\mathrm{i}k_2\gamma_y & 0 & \omega_d^2 + 0.25k_2\left(\frac{1}{3}\gamma_x^2 + \gamma_y^2\right) \end{bmatrix}. \tag{12}$$

Since $[p_+\ d_+\ p_-\ d_-] = [p_1\ p_2\ d_1\ d_2]Q$, where $Q = \begin{bmatrix} \frac{1}{\sqrt{2}} & 0 & \frac{1}{\sqrt{2}} & 0 \\ \frac{\mathrm{i}}{\sqrt{2}} & 0 & -\frac{\mathrm{i}}{\sqrt{2}} & 0 \\ 0 & \frac{1}{\sqrt{2}} & 0 & \frac{1}{\sqrt{2}} \\ 0 & \frac{\mathrm{i}}{\sqrt{2}} & 0 & -\frac{\mathrm{i}}{\sqrt{2}} \end{bmatrix}$, H_{NT} can be rewritten on the basis of $[p_+\ d_+\ p_-\ d_-]$,

$$H_{\mathrm{NT}}^s = Q^\dagger H_{\mathrm{NT}} Q. \tag{13}$$

Analogous to equation (11), on the $[p_+\ d_+\ p_-\ d_-]$ basis

$$H_{\mathrm{NT}}^s\begin{bmatrix} c_p^+ \\ c_d^+ \\ c_p^- \\ c_d^- \end{bmatrix} = \begin{bmatrix} \omega_+^2 & 0 & 0 & 0 \\ 0 & \omega_+^2 & 0 & 0 \\ 0 & 0 & \omega_-^2 & 0 \\ 0 & 0 & 0 & \omega_-^2 \end{bmatrix}\begin{bmatrix} c_p^+ \\ c_d^+ \\ c_p^- \\ c_d^- \end{bmatrix}. \tag{14}$$

We obtain

$$H_{\mathrm{NT}}^s = \begin{bmatrix} \omega_p^2 + F(\gamma_x^2 + \gamma_y^2) & A\gamma_+ & 0 & 0 \\ A^*\gamma_- & \omega_d^2 + E(\gamma_x^2 + \gamma_y^2) & 0 & 0 \\ 0 & 0 & \omega_p^2 + \mathrm{F}(\gamma_x^2 + \gamma_y^2) & A\gamma_- \\ 0 & 0 & A^*\gamma_+ & \omega_d^2 + E(\gamma_x^2 + \gamma_y^2) \end{bmatrix}, \tag{15}$$

where $\gamma_\pm = \gamma_y \pm \mathrm{i}\gamma_x$, A=0.2387ik_2, $E = \frac{k_2}{6}$, and $F = -0.1120k_2$.

If we set the reference energy level to be $\frac{1}{2}[\omega_p^2 + \omega_d^2 + (E + F)(\gamma_x^2 + \gamma_y^2)]$, equation (15) becomes

$$H_{\mathrm{NT}}^s = \begin{bmatrix} H_+ & 0 \\ 0 & H_- \end{bmatrix}, \tag{16}$$

with $H_\pm = \begin{bmatrix} -M + B\gamma^2 & A\gamma_\pm \\ A^*\gamma_\mp & M - B\gamma^2 \end{bmatrix}$, where $M = \frac{\omega_d^2 - \omega_p^2}{2}$, which is negative when $k_1 < k_2$, and $B = \frac{F-E}{2}$, which is also negative. Since H_{NT}^s has a similar formula as the Bernevig–Hughes–Zhang model [35], the spin Chern number can be calculated from equation (3). Since M and B are both negative, the spin Chern number for lattice with $k_1 < k_2$ is ± 1, which indicates it is topologically non-trivial.

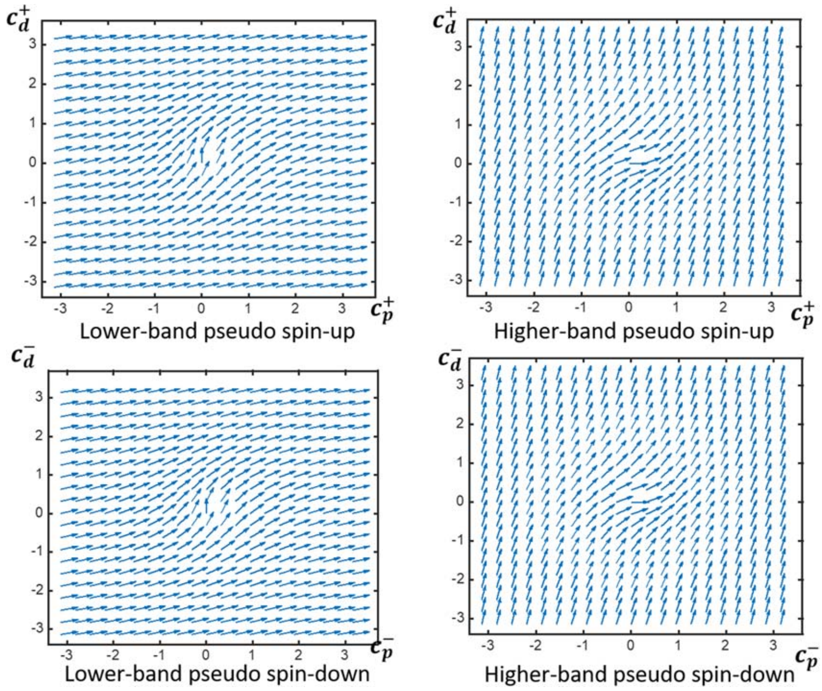

Figure 10. Projection of pseudo spin eigenvectors on $[p_+\ d_+\ p_-\ d_-]$ within the first Brillouin zone for lattice with $k_1 = 0.8$, $k_2 = 1$ and $m = 1$.

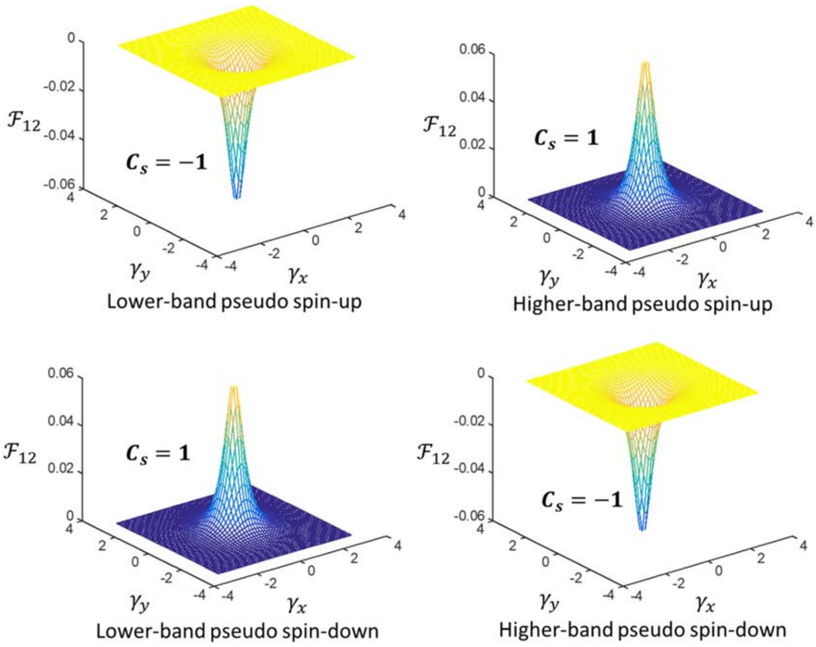

Figure 11. Berry Curvature and spin Chern number for pseudo spin channels for a lattice with $k_1 = 0.8$, $k_2 = 1$ and $m = 1$.

The projections of pseudo spin eigenvectors on $[p_+\ d_+\ p_-\ d_-]$ are plotted in figure 10. From figure 10 we can see that for the degenerate bands below the band gap, eigenvectors on most of the BZ are p-like, except for near the Γ point, where the eigenvectors are d-like. On the other hand, eigenvectors for the higher bands are more d-like near the Γ point and p-like elsewhere. The Berry curvature $\mathcal{F}_{12}(\gamma_x, \gamma_y)$ [37] for each of the pseudo spin channels are plotted in figure 11. By integrating the Berry curvature over the BZ [11]

$$C_s = \frac{1}{2\pi \mathrm{i}} \sum_{\gamma_x} \sum_{\gamma_y} \mathcal{F}_{12}(\gamma_x, \gamma_y) , \tag{17}$$

with values consistent with those previously obtained.

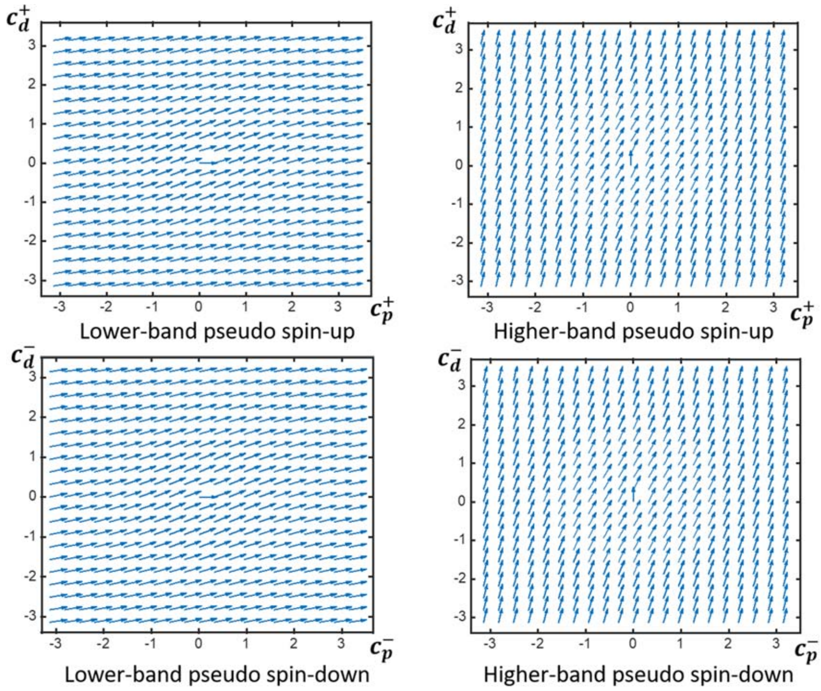

Figure 12. Projection of pseudo spin eigenvectors on $[p_+\ d_+\ p_-\ d_-]$ within the first Broullouin zone for lattice with $k_1 = 1.2$, $k_2 = 1$ and $m = 1$.

The Z_2 invariant is defined as $Z_2 = n_s\,(\mathrm{mod}\ 2)$, where $n_s = \frac{C_s^\uparrow - C_s^\downarrow}{2}$ is the quantum spin Hall conductivity [1]. The calculated spin Chern numbers $C_s^\uparrow$ and $C_s^\downarrow$ give $n_s = 1$, implying Z_2 is unity.

Similarly, for a lattice with $k_1 > k_2$, the effective spin Hamiltonian takes the same form as equation (16), but with $M > 0$, and $B < 0$. According to equation (3), $C_s = 0$, which proves that the lattice with $k_1 > k_2$ is topologically trivial. The projections of pseudo spin eigenvectors with $k_1 = 1.2$, $k_2 = 1$ and $m = 1$ are plotted in figure 12, which shows eigenvectors of the lower bands are more p-like, while eigenvectors to the higher bands tend to be d-like, as expected for an ordinary/trivial insulator.

Appendix D. Mini band gap due to C_6 symmetry breaking at the T–NT boundary

There would indeed be level repulsion/band anti-crossings (mini bandgap) when levels/bands of similar symmetry intersect, as would be relevant to the slight perturbation from C_6 symmetry at the boundary between the T and the NT regions. The magnitude of the gap could be related to the extent of asymmetry and could, in principle, be reduced, e.g. through minimizing the effect of C_6 symmetry breaking at the T–NT interface [37].

We indicate such influences in figure 13. The figures have differing relative mass ratios, and ratio of the inter-cell spring constant (T): intra-cell spring constant: inter-cell spring constant (NT). It can then be seen that as the asymmetry in mass and spring constants between the T and NT lattices increases, the mini band gap at the ‘crossing’ becomes larger as well.

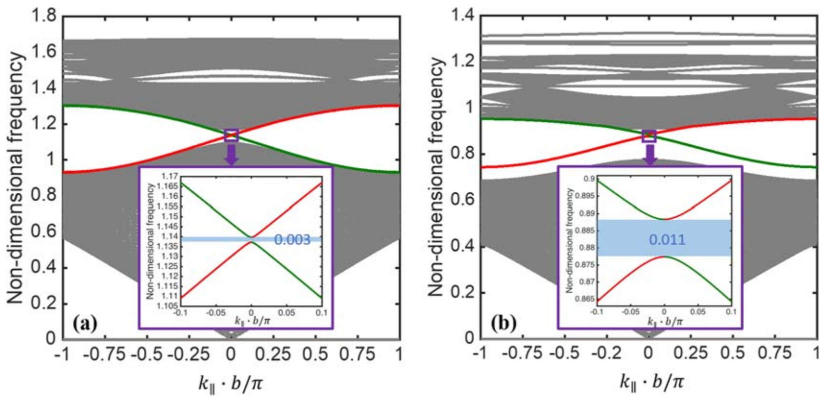

Figure 13. Mini bandgap at the crossing of the two helical modes for spring-mass lattices with (a) $\frac{m^{\mathrm{T}}}{m^{\mathrm{NT}}} = \frac{1.315}{1}$, and k_1^{T}: k_2: $k_1^{\mathrm{NT}} = 1.2$: 1: 0.8, and (b) $\frac{m^{\mathrm{T}}}{m^{\mathrm{NT}}} = \frac{2.8}{1}$, and k_1^{T}: k_2: $k_1^{\mathrm{NT}} = 1.55$: 1: 0.4.

References

[1] Hasan M Z and Kane C L 2010 Colloquium: topological insulators *Rev. Mod. Phys.* **82** 3045
[2] Qi X L and Zhang S C 2011 Topological insulators and superconductors *Rev. Mod. Phys.* **83** 1057
[3] Wang Z, Chong Y, Joannopoulos J D and Soljačić M 2008 Reflection-free one-way edge modes in a gyromagnetic photonic crystal *Phys. Rev. Lett.* **100** 013905
[4] Khanikaev A B, Mousavi S H, Tse W K, Kargarian M, MacDonald A H and Shvets G 2013 Photonic topological insulators *Nat. Mater.* **12** 233–9
[5] Ma T, Khanikaev A B, Mousavi S H and Shvets G 2015 Guiding electromagnetic waves around sharp corners: topologically protected photonic transport in metawaveguides *Phys. Rev. Lett.* **114** 127401
[6] Ma T and Shvets G 2016 All-Si valley-Hall photonic topological insulator *New J. Phys.* **18** 025012
[7] Lu L, Joannopoulos J D and Soljačić M 2014 Topological photonics *Nat. Photon.* **8** 821–9
[8] Wu L H and Hu X 2015 Scheme for achieving a topological photonic crystal by using dielectric material *Phys. Rev. Lett.* **114** 223901
[9] Ma T and Shvets G 2017 Scattering-free edge states between heterogeneous photonic topological insulators *Phys. Rev.* B **95** 165102
[10] Fleury R, Khanikaev A B and Alù A 2016 Floquet topological insulators for sound *Nat. Commun.* **7** 11744
[11] Wang P, Lu L and Bertoldi K 2015 Topological phononic crystals with one-way elastic edge waves *Phys. Rev. Lett.* **115** 104302
[12] Yang Z, Gao F, Shi X, Lin X, Gao Z, Chong Y and Zhang B 2015 Topological acoustics *Phys. Rev. Lett.* **114** 114301
[13] Xia B Z, Liu T T, Huang G L, Dai H Q, Jiao J R, Zang X G, Yu D J, Zheng S J and Liu J 2017 Topological phononic insulator with robust pseudospin-dependent transport *Phys. Rev.* B **96** 094106
[14] Khanikaev A B, Fleury R, Mousavi S H and Alù A 2015 Topologically robust sound propagation in an angular-momentum-biased graphene-like resonator lattice *Nat. Commun.* **6** 8260
[15] Deng Y, Ge H, Tian Y, Lu M and Jing Y 2017 Observation of zone folding induced acoustic topological insulators and the role of spin-mixing defects *Phys. Rev.* B **96** 184305
[16] Brendel C, Peano V, Painter O and Marquardt F 2018 Snowflake phononic topological insulator at the nanoscale *Phys. Rev.* B **97** 020102
[17] Mousavi S H, Khanikaev A B and Wang Z 2015 Topologically protected elastic waves in phononic metamaterials *Nat. Commun.* **6** 8682
[18] He C, Ni X, Ge H, Sun X C, Chen Y B, Lu M H, Liu X P and Chen Y F 2016 Acoustic topological insulator and robust one-way sound transport *Nat. Phys.* **12** 1124–9
[19] Haldane F D M 1988 Model for a quantum Hall effect without landau levels: condensed-matter realization of the 'Parity Anomaly' *Phys. Rev. Lett.* **61** 2015
[20] Thouless D J, Kohmoto M, Nightingale M P and Nijs M D 1982 Quantized Hall conductance in a two-dimensional periodic potential *Phys. Rev. Lett.* **49** 405
[21] Kane C L and Mele E J 2005 Quantum spin Hall effect in graphene *Phys. Rev. Lett.* **95** 226801
[22] Bernevig B A and Zhang S C 2006 Quantum spin Hall effect *Phys. Rev. Lett.* **96** 106802
[23] König M, Wiedmann S, Brüne C, Roth A, Buhmann H, Molenkamp L W, Qi X L and Zhang S C 2007 Quantum spin Hall insulator state in HgTe quantum wells *Science* **318** 766–70
[24] Rycerz A, Tworzydło J and Beenakker C 2007 Valley filter and valley valve in graphene *Nat. Phys.* **3** 172–5
[25] Xiao D, Yao W and Niu Q 2007 Valley-contrasting physics in graphene: magnetic moment and topological transport *Phys. Rev. Lett.* **99** 236809
[26] Kim Y, Choi K, Ihm J and Jin H 2014 Topological domain walls and quantum valley Hall effects in silicene *Phys. Rev.* B **89** 085429
[27] Lu J, Qiu C, Ke M and Liu Z 2016 Valley vortex states in sonic crystals *Phys. Rev. Lett.* **116** 093901
[28] Nash L M, Kleckner D, Read A, Vitelli V, Turner A M and Irvine W T M 2015 Topological mechanics of gyroscopic metamaterials *Proc. Natl Acad. Sci. USA* **112** 14495
[29] Pal R and Kand Ruzzene M 2017 Edge waves in plates with resonators: an elastic analogue of the quantum valley Hall effect *New J. Phys.* **19** 025001
[30] Wang Y T, Luan P G and Zhang S 2015 Coriolis force induced topological order for classical mechanical vibrations *New J. Phys.* **17** 073031
[31] Kariyado T and Hatsugai Y 2015 Manipulation of Dirac cones in mechanical graphene *Sci. Rep.* **5** 18107
[32] Süsstrunk R and Huber S D 2015 Observation of phononic helical edge states in a mechanical topological insulator *Science* **349** 47–50

[33] Zheng L Y, Theocharis G, Tournat V and Gusev V 2018 Quasitopological rotational waves in mechanical granular graphene *Phys. Rev.* B **97** 060101
[34] Dresselhaus M S, Dresselhaus G and Jorio A 2008 *Group Theory: Application to the Physics of Condensed Matter* (Berlin: Springer)
[35] Bernevig B A, Hughes T L and Zhang S C 2006 Quantum spin Hall effect and topological phase transition in HgTe quantum wells *Science* **314** 1757–61
[36] Johnson N F and Hui P M 1993 k.p theory of photonic band structures in periodic dielectrics *J. Phys.: Condens. Matter* **5** 2443
[37] Chaunsali R, Chen C W and Yang J 2018 Subwavelength and directional control of flexural waves in zone-folding induced topological plates *Phys. Rev.* B **97** 054307